Nanosecond-Flash ^{15}N Photo-CIDNP MAS NMR on Reaction Centers of *Rhodobacter sphaeroides* R26

Eugenio Daviso · Shipra Prakash · A. Alia ·
Peter Gast · Gunnar Jeschke · Jörg Matysik

Abstract Photochemically induced dynamic nuclear polarization (photo-CIDNP) is observed with time-resolved ^{15}N magic-angle spinning (MAS) nuclear magnetic resonance (NMR) in uniformly ^{15}N-labeled reaction centers (RCs) of the purple bacterium *Rhodobacter* (*Rb.*) *sphaeroides* R26 under illumination with nanosecond laser flashes. The ^{15}N NMR signals enhanced by the solid-state photo-CIDNP effect are related to electron spin densities in the primary radical pair and allow for reconstruction of the electronic structure at atomic scale. New assignments for the photochemically active nitrogens are proposed based on simulations of the intensities. The ratio of electron spin densities between cofactors P_L and P_M is observed to be about 4:1. The origin of the high asymmetry is discussed.

1 Introduction

The term "photochemically induced dynamic nuclear polarization" (photo-CIDNP) refers to the enhanced nuclear polarization which is caused by chemical processes involving radicals and is observed for example in ^{1}H, ^{13}C and ^{19}F nuclear magnetic resonance (NMR) experiments as negative (i.e. emissive) and enhanced positive (i.e. absorptive) signals during a light-induced or thermally activated reaction involving radical pairs (for reviews, see refs. [1–4]). In liquid-state NMR, the

E. Daviso · S. Prakash · A. Alia · J. Matysik (✉)
Institute of Chemistry, Leiden University, P.O. Box 9502, 2300 RA Leiden, The Netherlands
e-mail: j.matysik@chem.leidenuniv.nl

P. Gast
Institute of Physics, Leiden University, P.O. Box 9504, 2300 RA Leiden, The Netherlands

G. Jeschke
Laboratorium für Physikalische Chemie, Eidgenössische Technische Hochschule,
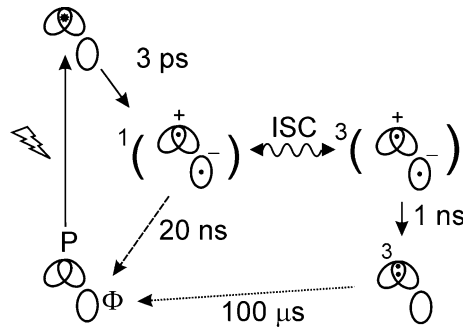Wolfgang-Pauli-Str. 10, 8093 Zürich, Switzerland

⚛ Springer

Fig. 1 Kinetics and spin dynamics of electron transport in quinone-depleted RCs of *Rb. sphaeroides* R26. After absorption of a photon, from the photochemically excited singlet state of the primary donor P*, an electron is transferred to the primary acceptor Φ, a bacteriopheophytin cofactor. This initial singlet radical pair $^1(P^+\Phi^-)$ is in a non-stationary state and highly electron polarized. An electron back-transfer leads to the electronic ground state (*dashed arrow*). Due to hyperfine interaction with nuclei, the singlet radical pair evolves into a triplet radical pair $^3(P^+\Phi^-)$. Concomitantly to this process of spin intersystem crossing (ISC), electron polarization is transferred to nuclei by the TSM and by the DD mechanisms. *Net* nuclear polarization is created by unbalancing the decay pathways of the singlet and the triplet radical pair (singlet and triplet branches). The DR occurs on signals of the donor since nuclear spin relaxation is significant during the molecular triplet state (^{3}P). In time-resolved resolved experiments, (TNP) can be observed directly from the singlet decay channel because the nuclear polarization of the triplet decay pathway (triplet branch, *dotted arrow*) reaches the ground state with a delay of 100 μs

phenomenon is often explained by the so-called radical pair mechanism [5, 6]. In the solid state, the occurrence of photo-CIDNP has been observed in frozen and quinone-blocked natural photosynthetic reaction centers (RCs) where it has first been detected by ^{15}N magic-angle spinning (MAS) NMR in 1994 [7]. Meanwhile, the effect has been observed under continuous irradiation of the sample by ^{13}C and ^{15}N MAS NMR in bacterial RCs of *Rhodobacter* (*Rb.*) *sphaeroides* WT [8] and R26 [9], *Rhodopseudomonas acidophila* [10], *Chlorobium tepidum* [11] and *Heliobacillus mobilis* [12] as well as in RCs of plant photosystems I and II [13–15]. Solid-state photo-CIDNP effects were also observed on ketones in organic phase [16].

The kinetics of the cyclic electron transfer in quinone-blocked RCs of *Rb. sphaeroides* R26 is described in Fig. 1. The radical pair is born in a pure electronic singlet state S_0, which evolves coherently into a triplet state T_0, while the other two triplet states (T_{+1} and T_{-1}) are not populated at high magnetic fields. This high electron polarization delocalized in the $S_0 - T_0$ manifold is detected as photochemically induced dynamic *electron* polarization [17, 18]. In this context, electron polarization of the radical pair corresponds to selective population of the two non-eigenstates having the magnetic quantum number $m = 0$ and being in the $S_0 - T_0$ manifold. In steady-state photo-CIDNP MAS NMR experiments, up to three mechanisms, two coherent and one based on relaxation, cause the build up of *net* photo-CIDNP [4, 8, 9, 19]: (1) In the three-spin mixing (TSM), the off-diagonal elements of the radical pair Hamiltonian lead to a transfer of polarization from the highly polarized electron pair to nuclei near a double matching condition [20, 21]. (2) In the differential decay (DD) mechanism, the different decay times of the

radical pair via either its singlet or its triplet state lead to additional nuclear polarization [22]. (3) In samples having a long lifetime of the molecular triplet state of the donor, as in RCs of *Rb. sphaeroides* R26, the differential relaxation (DR) mechanism leads to relaxation of nuclear polarization in the decay pathway of the triplet state of the radical pair which causes *net* nuclear polarization in the electronic ground state [4, 23, 24]. The enhancement of signal sensitivity and selectivity of the nuclei allows for detailed studies on structure and dynamics of the photosynthetic cofactors active in the formation of the primary radical pair [4]. The observed chemical shifts are related to the electronic ground state of the cofactors and, in absence of spin diffusion, the photo-CIDNP intensities are related to the local electron spin densities. While ^{13}C photo-CIDNP MAS NMR provides complex spectra which mostly do not allow for a straightforward chemical shift assignment, ^{15}N photo-CIDNP MAS NMR data are less complex and thus allow for more direct assignment and interpretation.

Recent development of time-resolved nanosecond laser flash photo-CIDNP MAS NMR allows to observe the evolution of nuclear polarization on the micro- and millisecond time scale [25, 26]. In such time-resolved ^{13}C photo-CIDNP MAS NMR experiments, due to the difference in the two decay pathways of the radical pair, transient nuclear polarization (TNP) and nuclear spin diffusion have been observed [4, 25, 26]. These studies are also very suited to reveal the mechanisms involved in the solid-state photo-CIDNP effect [4, 26]. Here, we present time-resolved ^{15}N photo-CIDNP MAS NMR data obtained on RCs of *Rb. sphaeroides* R26.

2 Materials and Methods

2.1 Reaction Center Preparation

Rhodobacter sphaeroides R26 was grown under anaerobic conditions in a medium containing 95% ^{15}N-labeled NH$_4$Cl from VEB Berlin Chemie (Berlin-Adlershof, Germany) [27, 28]. The extent of ^{15}N incorporation has been determined by gas chromatograph and mass spectrometer (GC-MS) to be $\sim$60%. The RCs were isolated by the procedure described in ref. [29]. Quinone depletion in the WT RC is reported in ref. [8]. For quinone reduction in R26 RC, 5 μL of 0.05 M sodium dithionite has been added to 100 μL of sample volume.

2.2 MAS NMR Measurements

The NMR experiments were performed using an AV-200 NMR spectrometer (Bruker Biospin, Karlsruhe, Germany). The samples were loaded into optically transparent 4-mm sapphire rotors. For continuous illumination experiments, a setup specially designed for the Bruker MAS probe has been applied [4, 30]. Light and dark spectra were obtained by simple Bloch decay followed by a spin echo pulse sequence. The cycle delay for continuous illumination experiments was 4 s.

Time-resolved nanosecond-flash photo-CIDNP MAS NMR measurements have been performed as in ref. [25] by changing the delay time between laser light pulse

excitation and NMR detection systematically from 0 to 500 ms in ^{15}N-labeled RCs of *Rb. sphaeroides* R26 ^{15}N labeled. The cycle delay was 134 ms.

In all experiments, the signal has been detected using two-pulse phase modulation (TPPM) proton decoupling [31]. The temperature has been 233 K at a spinning frequency of 8 kHz. Artificial line broadening of 40 Hz has been applied. The number of scans was 120 k per spectrum. Chemical shifts are given relative to ^{15}NH$_3$, using the response of solid ^{15}NH$_4$NO$_3$ at $\delta = 23.5$ ppm as a reference.

2.3 Spectral Fitting of Experimental Data

The fitting of the experimental photo-CIDNP MAS NMR spectrum of RCs of *Rb. sphaeroides* R26 has been performed using Igor Pro v. 6.01 (Lake Oswego, OR, USA). As starting parameters for the fitting procedure, the chemical shifts have been taken from the literature [32]. During the fitting procedures, the chemical shifts have been kept fixed for all the spectra collected at different evolution times.

In Table 1, the values of the normalized NMR intensities for both P_L and P_M are:

$$\tilde{p}_i = p_i/p_k$$

where p_k is the highest value of p_i, being P_L-NIV.

Table 1 Comparison of local electron spin densities within the radical pair of RCs of *Rb. sphaeroides* R26

IUPAC number	Simulation[a]		Experiments		
	Normalized photo-CIDNP ^{15}N intensity	Fermi contact (a_{iso})	Normalized photo-CIDNP ^{15}N intensity[a]	Fermi contact (a_{iso}) by ^{15}N-ESEEM[b]	Fermi contact (a_{iso}) by ^{15}N cw-ENDOR[c]
P_L-NI	−0.6	0.95	−0.7	2.61	2.40
P_L-NII	−0.8	1.41	−0.7	3.72	3.24
P_L-NIII	−0.4	0.84	−1.0	3.49	2.93
P_L-NIV	−0.9	1.78	−1.0	2.97	2.68
P_M-NI	−0.3	0.57	−0.1	0.55	1.29
P_M-NII	−0.5	0.91	−0.2	0.74	1.59
P_M-NIII	−0.4	0.72	−0.3	0.52	1.28
P_M-NIV	−0.6	1.10	−0.3	0.68	1.30
BPheo- NII	−0.5	0.71	−0.1		
BPheo-NIV	−1.0	0.70	−0.9		
Ratio ρ_L/ρ_M	1.5	1.5	3.8	5.1	2.1

IUPAC International Union of Pure and Applied Chemistry

Isotropic hyperfine interaction (a_{iso}) values are given in megahertz. The ratio ρ_L/ρ_M is defined by the ratio of the electron spin densities ρ of cofactors P_L and P_M, expressed either by transient photo-CIDNP intensities or by isotropic hyperfine interaction values

[a] This work

[b] Ref. [53]

[c] Ref. [54]

2.4 Density Functional Theory (DFT) Calculations of the Hyperfine Tensors

DFT computations of hyperfine (hf) coupling tensors were performed with the Amsterdam Density Functional (ADF) 2002.1 package (SCM N.V., Amsterdam, The Netherlands), using the triple-zeta polarized (TZP) all-electron basis set for all atoms as described before [19]. Geometries of ground state molecules were taken from the crystal structure in the charge-neutral state [Protein Data Bank (PDB) identifier, 1AIJ] [33] and subjected to geometry optimization within ADF in the cation radical state in vacuo. Such geometry optimization converges to the local minimum of the energy hypersurface that is next to the experimental structure, so that side group conformations and deformations of the macrocycles are preserved. The computations were performed considering P_L and P_M coordinated with His-L173 and His-M202 to the Mg atom and with the phytyl chain substituted by a methyl group.

The ^{15}N hyperfine tensors have been obtained by scaling the ^{14}N hyperfine tensors, originally computed by ADF, with the ratio of the nuclear g values $g_n($[15]N$)/g_n($[14]N$)$. Details on the DFT calculations are provided in refs. [4, 19, 26].

2.5 Numerical Simulations of the TNP Intensities

The photo-CIDNP intensities have been computed using Matlab[TM] (The Math-Works, Inc., Natick, MA, USA). The theory used for simulation is presented in Sect. 4.3. Full powder average describing all interactions by tensors is applied. A spherical grid, function *sphgrid* in EasySpin [34], with 16 knots and C_i symmetry (481 orientations), has been found to be sufficient for powder averaging. The Matlab routine will be provided upon request. Details of the simulations are described in [4, 19, 26]. Differences between experimental and simulated data are mainly due to imprecision of DFT calculations as well as the estimation of the g tensor of the bacteriopheophytin acceptor. Furthermore, the error margins are rather large for the exchange and the electron–electron dipole coupling in the radical pair. The computed values have been used as input file for SpinEvolution [35] to simulate the MAS spin echo pulse sequence adopted in the NMR experiments.

The simulated nuclear polarizations presented in Table 1 are normalized by:

$$\tilde{a}_i = a_i/a_k$$

where a_k is the highest value of the a_i terms of ^{13}N, being N-II of BPheo.

3 Results

3.1 Continuous Illumination Experiments

Figure 2A is the ^{15}N MAS NMR spectrum of uniformly ^{15}N-labeled RCs of *Rb. sphaeroides* R26 RC sample obtained in the dark. The weak and broad positive signals arising at about 120 ppm originate from amide nitrogens of the protein backbone. Figure 2B is a ^{15}N photo-CIDNP MAS NMR spectrum of the same sample collected under continuous illumination with white light. Upon fitting (not

shown), a total of ten photo-CIDNP induced signals can be resolved in the spectrum. Due to the moderate magnetic field strength, no spinning sidebands are observed, while they have been identified in previous ^{15}N photo-CIDNP MAS NMR experiments at higher fields and lower MAS frequencies [4, 7, 27, 36]. The full width at half height (FWHH) of 40–50 Hz are in line with the concept of a rigid and well-ordered inner part of the RC [37], as it is required for highly efficient electron transfer. No major differences have been observed considering the width of the signals arising from the donor and the acceptor.

3.2 Nuclear Polarization Evolution

The spectra C–L of Fig. 2 have been obtained in the dark (C) and with time-resolved photo-CIDNP MAS NMR by applying different time delays of 0 μs (D), 20 μs (E), 80 μs (F), 160 μs (G), 4 ms (H), 10 ms (I) and 500 ms (L) between the light pulse and the NMR detection pulse using a 532-nm 8-ns light flash. All the spectra have been collected at a magnetic field of 4.7 T and a temperature of 233 K. The data show the time-dependent evolution of ^{15}N nuclear polarization occurring in the radical pair. In the initial stage, as shown in the spectrum obtained with a delay time of 0 μs (D), all light-induced signals have their maximum intensities. During the following evolution, the intensities of all signals of the spectrum decay, especially of the two groups of signals between 180 and 200 ppm as well as between 290 and 300 ppm. After about 160 μs (G), these groups of signals are

Fig. 2 ^{15}N photo-CIDNP MAS NMR spectra of uniformly ^{15}N-labeled RCs of *Rhodobacter sphaeroides* R26 in the dark (*A*) and under continuous illumination (*B*). The spectra C–L have been obtained in the dark (*C*) and with different time delays of 0 μs (*D*), 20 μs (*E*), 80 μs (*F*), 160 μs (*G*), 4 ms (*H*), 10 ms (*I*) and 500 ms (*L*) between the light pulse and the NMR detection pulse using a 532-nm 8-ns flash. All the spectra have been collected at a magnetic field of 4.7 T and a temperature of 233 K
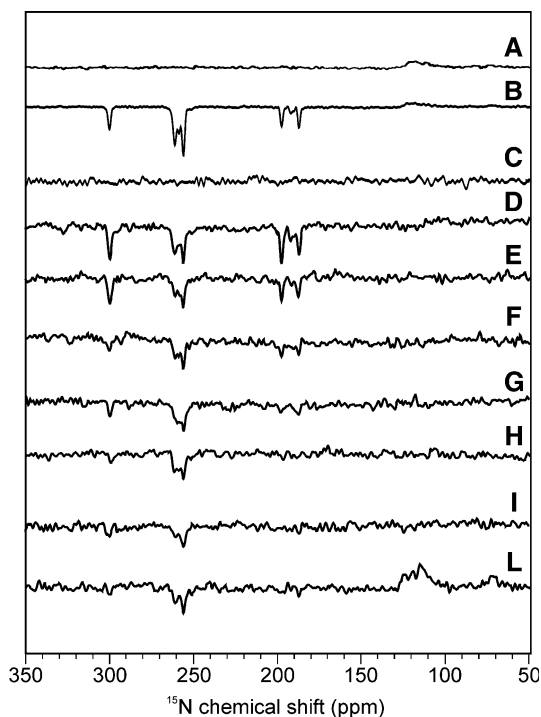
hardly observed, while the central group of signals between 250 and 260 ppm remains on the millisecond time scale. Hence, it appears that (TNP) associated with the two outer groups of signals occurs on the microsecond time scale, while the dominant central group of signals survives in the millisecond time regime.

In the previous works [4, 8, 38], the solid-state photo-CIDNP effect occurring under continuous illumination have been explained by the TSM, DD, and DR mechanisms. TNP also has been observed recently by time-resolved ^{13}C photo-CIDNP MAS NMR on RCs of *Rb. sphaeroides* WT and R26 [26]. In R26 samples, the ^{13}C TNP also decayed on the microsecond time scale. As shown in Fig. 1, the decay of the singlet branch of the radical pair occurs in 20 ns, while the nuclear polarization originating from the triplet state of the radical pair reaches the ground state after 100 μs. Hence, the lifetime of the TNP is in the microsecond range and correlates to the lifetime of the molecular triplet state of the donor (^{3}P). It has been shown that the strong paramagnetic line broadening for nuclei exposed to the strong local magnetic field of the triplet electrons hides the NMR signals from this fraction of RCs [26]. Hence, the delayed observability of RCs from the triplet branch allows for transient selective observation of the RCs of the singlet branch. After the RCs from the triplet branch have returned to the ground state, their opposite nuclear polarization extinguishes the TNP signal.

4 Discussion

4.1 Sign of the Signals

The sign of a TNP signal $\Gamma(i)$ for nucleus i follows the multiplicative sign rules of the radical pair mechanism [39] and is given by the product of four signs:

$$\Gamma(i) = \mu \cdot \varepsilon \cdot \text{sgn}(\gamma_n) \cdot \text{sgn}(\Delta g) \cdot \text{sgn}(A_i)$$

where $\text{sgn}(\gamma_n)$ is the sign of the gyromagnetic ratio of the nucleus (negative for ^{15}N), $\text{sgn}(A_i)$ is the sign of the difference of the *g* values of the radicals, and $\text{sgn}(A_i)$ the sign of the secular hyperfine interaction. Furthermore, μ is "+" for a triplet precursor and "−" for a singlet precursor, and ε is "+" for recombination products, corresponding to the singlet decay branch, and "−" for escape products, corresponding to the triplet decay branch. If only this solid-state equivalent of the radical pair mechanism is operative, the polarization of RCs in the singlet branch has the same magnitude as the one of RCs in the triplet branch and opposite sign. Hence, when all RCs have returned to the ground state, the ground state nuclear polarization exactly cancels. For this reason, only the nuclear polarization can be observed transiently during the time when single-branch RCs have already returned to the ground state while triplet branch RCs have not. The NMR signals from the triplet branch RCs are then suppressed by strong paramagnetic line broadening. The TNP thus arises solely from the singlet branch, so that the product $\mu \cdot \varepsilon$ has a negative sign.

In general, the sign of Δg in RCs depends on orientation. However, given the *g* tensors of donor and acceptor radicals known from high-field EPR spectroscopy [40, 41], for an overwhelming majority of orientations it is positive in the spin

Hamiltonian for acceptor nuclei and negative for donor nuclei. The opposite sign ensues as we assume that the nucleus is coupled to the first electron spin and $\Delta g = g_1 - g_2$ [19]. The sign of A_i may also depend on orientation, but anisotropic contributions to the radical pair mechanism (RPM) average to a first approximation. Hence, the sign of the isotropic hyperfine coupling determines whether the polarization is emissive [negative $\Gamma(i)$) or absorptive (positive $\Gamma(i)$]. For all donor ^{15}N nuclei the isotropic hyperfine coupling is positive, so that emissive signals are expected. The acceptor ^{15}N nuclei in rings I and III, which carry the protons and have the smallest chemical shifts among all light-induced signals in the spectra, have positive isotropic hyperfine couplings. Because of the positive sign of Δg for the acceptor, absorptive signals are expected for these nuclei. Such absorptive signals are not observed. According to the work of Zysmilich and McDermott [42] they should appear in the shift range between about 100 and 110 ppm, where we do not observe any signals. In contrast, the acceptor ^{15}N nuclei in rings II and IV have negative isotropic hyperfine couplings, so that emissive signals are expected.

4.2 Signal Assignment to Donor and Acceptor Cofactors

Since all photo-CIDNP signals are emissive, we may only exclude the N_I and N_{III} of the acceptor, but cannot distinguish between donor nuclei and acceptor nuclei N_{II} and N_{IV} by considering the sign of the signals only. The chemical shift information, however, allows clearly to distinguish signals from bacteriochlorophylls (BChl) from those of bacteriopheophytins (BPhe). McDermott and co-workers [42] assigned the "outer" set of signals (130–150 and 290–310 ppm) to BPhe and the "inner" set to BChl. These authors, however, did not aim to assign the signals of BChl to either P_L or P_M, the two cofactors of the special pair donor. Later, based on the simple assumption of a link between continuous illumination photo-CIDNP intensities and local electron spin densities, it was suggested that the signals which are higher in the continuous illumination experiment are originating from the P_L cofactor known to carry electron spin density higher than P_M [8, 43]. This relation holds indeed for the TSM-induced polarization that is proportional to the square of spin densities in the corresponding atomic p orbitals that contribute to the singly occupied molecular orbital (SOMO) [44]. However, it is not clear whether this argument extends to TNP, which is roughly proportional to spin densities in the corresponding atomic s orbitals that contribute to the SOMO. Furthermore, under continuous illumination spin diffusion and relaxation effects may establish steady-state polarizations that do not follow such simple rules. In the present paper, we re-investigate these assignments on basis of new ^{15}N data from model compounds [32] and of simulations of the local nuclear polarization occurring transiently from the singlet state of the radical pair. As shown in Sect. 4.3, these TNP intensities can be taken as approximation for local electron spin densities.

4.3 Simulation of TNP Signal Intensities

The occurrence of the TNP [26] is not specific for solid-state photo-CIDNP but it is closely related to the classical radical pair mechanism [26] in which spin-sorting

occurs in the radical pair due to isotropic hf interaction. This TNP can either be detected with time-resolved NMR, or it can be detected in static NMR experiments if the reaction products of the singlet and the triplet states of the radical pair are chemically distinguished.

In any case, the system starts from a pure singlet electronic state described by the following density matrix for a fictitious spin $S' = 1/2$ corresponding to only the ST_0 manifold:

$$\sigma_0 = \frac{1}{2}E - S'_x, \tag{1}$$

where E is the identity operator and $-S'_x$ is the operator representing the singlet state of the fictitious electron spin [20]. The triplet state is represented by $+S'_x$.

When the radical is born, the radical pair Hamiltonian is described by:

$$H_{ST_0} = \Delta\Omega S'_z + \omega_I I_z + A_{zz}S'_z I_z + B_{zx}S'_z I_x + B_{zy}S'_z I_y - dS'_x, \tag{2}$$

where the $\Delta\Omega$ is the difference of the electron Zeeman interactions of the two electron spins, ω_I is the nuclear Zeeman interaction, A_{zz} represents the secular hf coupling and B_{zx} and B_{zy} are the pseudosecular hf couplings and $d = 2J + d'$ is the total coupling between the two electron spins, with J the exchange coupling and d' the dipole–dipole coupling.

The lifetime of the radical pair depends on the singlet and triplets decay rates from the singlet and triplet branch as described in Fig. 1. The singlet state of the radical decays to the ground state in 20 ns, while the triplet state of the radical decays to the molecular triplet state of the donor in 1 ns. TNP is the polarization in RCs that is stored in the electronic ground state via the singlet decay branch. The NMR signals of nuclei of RCs with a triplet donor are broadened beyond detection.

Intersystem crossing in the radical pair state is computed by propagating the density matrix according to

$$\sigma_{S_0T_0} = e^{-iH_{S_0T_0}t}\sigma_0\, e^{+iH_{S_0T_0}t}. \tag{3}$$

In the ground state, all interactions except for the nuclear Zeeman interaction vanish due to extinction of the electron spins, so that the Hamiltonian is given by:

$$H_{GS} = \omega_I I_z. \tag{4}$$

The part of the density matrix that decays to the ground state via the singlet (σ_s) is projected out as described in ref. [24] using projection operators for the fictitious spin [19], stored and propagated according to:

$$\sigma_S(t) = e^{-iH_D t}\sigma_0\, e^{+iH_D t}. \tag{5}$$

Nuclear polarization occurring in the TNP is therefore related to the singlet part of the density matrix by:

$$np = Tr\{I_z\sigma_S(t_{20})\}, \tag{6}$$

where t_{20} is the lifetime of the singlet pair decay.

In the limit of short evolution times in the radical pair state, considerations along the lines given in ref. [21] suggest that the polarization arising selectively from the

S state (TNP) is linearly proportional to the secular hyperfine interaction. In the same limit, the orientation average of polarization from the purely anisotropic secular hyperfine coupling vanishes. Hence, signal intensities are roughly proportional to the isotropic hyperfine couplings a_{iso} and therefore to local electron spin densities in atomic s orbitals that contribute to the SOMO [4, 26].

4.4 Simulation-based Assignment of Individual Signals

Due to the proportionality between the local isotropic electron spin densities occurring in the singlet state of the radical pair and the TNP signal intensities, the initially observed photo-CIDNP polarization can be used for the assignment of signals. Therefore, we simulated the isotropic electron spin densities for all nitrogen atoms of the three cofactors forming the radical pair (Table 1). On the other hand, we use for the assignments the initial ^{15}N photo-CIDNP MAS NMR spectrum (spectrum D in Fig. 2), in which the light-induced signals are mainly due to TNP. In order to obtain the ^{15}N chemical shift values and intensities (Table 1), we fitted the experimental intensities with Lorentz functions on the basis of earlier continuous illumination ^{15}N photo-CIDNP MAS NMR experiments having better signal-to-noise ratio [4].

Figure 3 compares the resulting simulated TNP spectrum (spectrum A) and the experimentally observed initial ^{15}N photo-CIDNP MAS NMR spectrum (spectrum B, identical with spectrum D in Fig. 2). Table 2 contains the chemical shift assignments from isolated cofactors [32] as well as the new assignments obtained on RCs from *Rb. sphaeroides*.

The experimental spectrum shows at around 300 ppm a strong signal (299.7 ppm) accompanied by a weak one (295.0 ppm). Both signals originate from the BPheo acceptor. Intensity simulations show that the stronger signal is caused by N-IV, while the weaker originates from N-II. Such assignment is also in line with
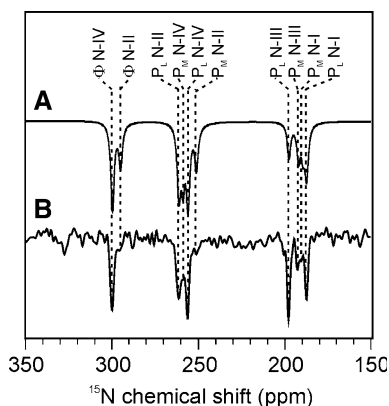

Fig. 3 *A* Simulated ^{15}N photo-CIDNP MAS NMR spectrum obtained by calculating initial ^{15}N photo-CIDNP intensities (for details, see Sect. 4.3). The calculated signals have been assigned to experimentally obtained chemicals shifts (Table 2). *B* Experimental nanosecond laser flash ^{15}N photo-CIDNP MAS NMR spectrum of uniformly ^{15}N-labeled RCs of *Rhodobacter sphaeroides* R26 obtained with a time delay of 0 μs between the light pulse and the NMR detection pulse using a 532-nm 8-ns flash (identical with spectrum *D* in Fig. 2)

Table 2 Experimental ^{15}N NMR chemical shifts obtained from solid samples of isolated BChl *a* and BPheo *a*

IUPAC number	^{15}N chemical shift[a] (ppm)	^{15}N chemical shift[b] (ppm)
P_L-NI	191.8	187.2
P_M-NI		189.3
P_L-NII	258.3	261.2
P_M-NII		251.0
P_L-NIII	196.9	197.4
P_M-NIII		191.9
P_L-NIV	258.3	255.9
P_M-NIV		258.8
BPheo- NII	296.1	295.0
BPheo-NIV	303.2	299.7

IUPAC International Union of Pure and Applied Chemistry

[a] Ref. [32]

[b] This work

the chemical shift data of the isolated cofactors [32] showing for N-IV a higher ppm value as for N-II.

The group of signals between 270 and 250 ppm is composed by four signals composed by the N-II and N-IV nitrogens of P_L and P_M. All signals have rather similar intensities, unfortunately also the ppm values coincide in the model compound study [32].

The intensity simulations however suggest that both signals from P_L have higher intensity than those of P_M. The highest signal originates from the N-IV of P_L. In the simulations, the N-II of P_M is clearly the weakest of these signals and can therefore conveniently be assigned to the experimental peak at 251.0 ppm.

Also the group of signals between 200 and 180 ppm is composed of four signals, originating from N-I and N-III from P_L and P_M. The chemical shifts of the isolated BChl suggest that N-III appears at about 5 ppm higher ppm values than N-I (Table 2). The strongest signal (197.4 ppm) is clearly assigned to N-III of P_L and the second strongest to N-I of P_M. Due to ppm value and intensity, the weak signal of N-III of P_M is assigned to higher ppm values compared to that of N-I of P_L.

The general similarity of the experimental and the simulated spectra suggests that the anisotropic contributions can indeed be neglected. Deviations of the observed amplitude between experiment and simulation are also caused by errors in the DFT computation of hyperfine couplings and uncertainties in the experimentally determined magnetic parameters of the radical pair (g tensors, dipole–dipole coupling, exchange coupling).

4.5 Electron Spin Density Distribution Between P_L and P_M

Table 1 contains the TNP intensities of all eight donor nitrogens. Using them to determine experimentally the electron spin density (ρ) distribution on both cofactors on the molecular scale (ρ_L/ρ_M), we find a ratio of almost 4:1 in favor of P_L over P_M. This experimental value suggests significantly more asymmetry on the molecular scale than predicted by the simulations. Also previous steady-state ^{13}C photo-CIDNP

MAS NMR experiments suggested a much more balanced distribution of 3:2 [8]. The question arises why time-resolved ^{15}N photo-CIDNP MAS NMR experiments lead to observation of such unexpected asymmetry.

4.6 Comparison to ^{15}N-ENDOR and ESEEM Experiments

Electron spin densities on the nitrogen atoms of the special pair have also been measured with various EPR methods as electron-nuclear double resonance (ENDOR) and electron spin echo envelope modulation (ESEEM). It turned out, however, that ENDOR on the quadrupole nucleus ^{14}N is difficult [45]. For nuclei having small Larmor frequencies and hyperfine couplings, ESEEM leads to better results. Initial one-dimensional (1-D) ^{15}N-ESEEM experiments could only detect four of the eight nitrogen atoms of the special pair [46–52]. A careful study using different advanced ESEEM techniques, such as hyperfine sublevel correlation (HYSCORE) spectroscopy [53], allowed observing for the first time all eight nitrogen positions and obtaining complete sets of their principle values of their hyperfine tensors. The experimental results obtained at 20 K show that the electron spin density is on a ratio of 5:1 in favor of the four nitrogens assigned to P_L over those assigned to P_M. This result is well in line with the results presented above obtained with ^{15}N time-resolved photo-CIDNP MAS NMR at 233 K.

On the other hand, the experimental ^{1}H ENDOR [43], ^{15}N ENDOR [54] and ^{13}C steady-state photo-CIDNP MAS NMR data [8] show clearly a distribution of electron spin density about 2:1 in favor of P_L, which is also in line with the calculations. Both photo-CIDNP experiments on ^{13}C and ^{15}N have been measured at the same temperature, suggesting that the difference between the two observations is not caused by a temperature-dependent effect. Similarly, both experiments have been done with quinone-depleted samples prepared in the same buffers and using the same detergents.

One may assume that the difference could also be due to the difference in time scales of the various experiments. While ^{13}C steady-state photo-CIDNP MAS NMR data [8] show the distribution of 2:1, ^{15}N laser flash experiments lead to 4:1. The value of 5:1, however, has been found by 2-D ESEEM also in a sample under continuous illumination and not under flash-light conditions [53].

Differences between samples frozen under continuous illumination and samples frozen in the dark are known for the acceptor site [33, 55]. Indeed, continuous illumination photo-CIDNP MAS NMR has been measured on light-frozen samples, while laser flash experiments were done on samples frozen in the dark. On the other hand, these structural effects cannot explain the observed differences in distribution of electron spin densities because all samples used for ENDOR and ESEEM have been frozen under illumination.

It is also possible that exclusive consideration of the four nitrogens is too selective to measure the electron spin density distributions between the entire two cofactors. In this case, however, the ^{15}N continuous-wave ENDOR experiments [54] also should have shown a more asymmetric ratio. Future ^{13}C time-resolved photo-CIDNP MAS NMR experiments obtained under same conditions may provide the full picture at the atomic resolution and may allow to explain the differences observed.

5 Outlook

Only a few natural RCs have been studied as extensively as that of the purple bacterium *Rb. sphaeroides*. The RCs of the overwhelming majority of photosynthetic organisms have not been isolated and spectroscopically or structurally characterized. The current canon of RCs shows a great variation of electronic properties at both, donor and acceptor side. Donors have been found to be monomers, asymmetric dimers and symmetric dimers [56]. Also the involvement of the protein matrix in the donor structure has been proposed [12, 15]. Two parallel branches have been proposed on the acceptor site [57]. For understanding the principles of light reaction of photosynthesis, one would like to be not dependent on the small number of RCs which have been found out accidentally to be easy to grow, to isolate, to label or to crystallize. A robust method to analyze electronic structures of various RCs without sophisticated sample preparation is required.

It has been shown that high-quality photo-CIDNP data can be obtained from membrane-bound RCs [12] and even cells [9]. Hence, even if an RC isolation is not feasible, photo-CIDNP MAS NMR still can be applied. In this paper, it also has been demonstrated that from uniformly ^{15}N-labeled RCs, a detailed analysis of the electronic structures as well as of the kinetics of the photochemical machinery is possible. Since uniform ^{15}N labeling is rather easy to achieve, photo-CIDNP MAS NMR on uniformly ^{15}N-labeled and reduced membranes and cells may provide an option for fast screening of functional properties of RC from various photosynthetic organisms.

References

1. P.J. Hore, R.W. Broadhurst, Prog. Nucl. Magn. Reson. Spectrosc. **25**, 345–402 (1993)
2. H.D. Roth, in *Encyclopedia of Nuclear Magnetic Resonance*, vol. II, ed. by D.M. Grant, R.K. Harris (Wiley, Chichester, 1996), pp. 1337–1350
3. M. Goez, in *Advance in Photochemistry*, ed. by D.C. Neckers, D.H. Volman, G. von Bönau (Wiley, New York, 1997), pp. 63–163
4. E. Daviso, Doctoral Thesis, Leiden University, Leiden, The Netherlands, (2008). https://openaccess.leidenuniv.nl/handle/1887/13264
5. G.L. Closs, L.E. Closs, J. Am. Chem. Soc. **91**, 4549–4550 (1969)
6. R. Kaptein, J.L. Oosterhoff, Chem. Phys. Lett. **4**, 195 (1969)
7. M.G. Zysmilich, A. McDermott, J. Am. Chem. Soc. **116**, 8362–8363 (1994)
8. S. Prakash, A. Alia, P. Gast, H.J.M. de Groot, G. Jeschke, J. Matysik, J. Am. Chem. Soc. **127**, 14290–14298 (2005)

9. S. Prakash, A. Alia, P. Gast, H.J.M. de Groot, J. Matysik, G. Jeschke, J. Am. Chem. Soc. **128**, 12794–12799 (2006)
10. A. Diller, P. Gast, G. Jeschke, A. Alia, J. Matysik, in *Energy from the Sun*, ed. by J. Allen, E. Gantt, J. Golbeck, B. Osmond (Springer, Dordrecht, 2008), pp. 10606–10614
11. E. Roy, A. Alia, P. Gast, H. van Gorkom, H.J.M. de Groot, G. Jeschke, J. Matysik, Biochim. Biophys. Acta **1767**, 610–615 (2007)
12. E. Roy, T. Rohmer, P. Gast, G. Jeschke, A. Alia, J. Matysik, Biochemistry **47**, 4629–4635 (2008)
13. J. Matysik, A. Alia, P. Gast, H.J. van Gorkom, A.J. Hoff, H.J.M. de Groot, Proc. Natl. Acad. Sci. USA. **97**, 9865–9870 (2000)
14. A. Alia, E. Roy, P. Gast, H.J. van Gorkom, H.J.M. de Groot, G. Jeschke, J. Matysik, J. Am. Chem. Soc. **126**, 12819–12826 (2004)
15. A. Diller, E. Roy, P. Gast, H.J. van Gorkom, H.J.M. de Groot, C. Glaubitz, G. Jeschke, J. Matysik, A. Alia, Proc. Natl. Acad. Sci. USA. **104**, 12767–12771 (2007)
16. K. Miesel, A.V. Yurkovskaya, H.M. Vieth, Appl. Magn. Res. **26**, 51–64 (2004)
17. A.J. Hoff, Q. Rev. Biophys. **17**, 153–282 (1984)
18. A.J. Hoff, J. Deisenhofer, Phys. Rep. **287**, 2–247 (1997)
19. G. Jeschke, J. Matysik, Chem. Phys. **294**, 239–255 (2003)
20. G. Jeschke, J. Chem. Phys. **106**, 10072–10086 (1997)
21. G. Jeschke, J. Am. Chem. Soc. **120**, 4425–4429 (1998)
22. A. McDermott, M.G. Zysmilich, T. Polenova, Solid State Nucl. Magn. Reson. **11**, 21–47 (1998)
23. R.A. Goldstein, S.G. Boxer, Biophys. J. **51**, 937–946 (1987)
24. T. Polenova, A.E. McDermott, J. Phys. Chem. B **103**, 535–548 (1999)
25. E. Daviso, A. Diller, A. Alia, J. Matysik, G. Jeschke, J. Magn. Reson. **190**, 43–51 (2008)
26. E. Daviso, A. Alia, S. Prakash, A. Diller, P. Gast, J. Lugtenburg, J. Matysik, G. Jeschke, J. Phys. Chem. C **113**, 10269–10278 (2009)
27. S. Prakash, S.H. Tong, A. Alia, P. Gast, H.J.M. de Groot, G. Jeschke, J. Matysik, in *Photosynthesis: Fundamental Aspect to Global Perspectives*, A. ed. by van der Est, A. Bruce (Allen Press, Montreal, 2005) pp. 236–237
28. E. Daviso, K.B.S. Sankar Gupta, S. Prakash, A. Alia, P. Gast, G. Jeschke, J. Matysik, in *Energy from the Sun*, ed. by J. Allen, E. Gantt, J. Golbeck, B. Osmond (Springer, Dordrecht, 2008) pp. 63–66
29. G. Feher, M.Y. Okamura, in *The Photosynthetic Bacteria*, ed. by R.K. Clayton, W. Sistrom (Plenum Press, New York, 1978), pp. 349–378
30. J. Matysik, E. Schulten, A. Alia, P. Gast, J. Raap, J. Lugtenburg, A.J. Hoff, H.J.M. de Groot, Biol. Chem. **382**, 1271–1276 (2001)
31. A.E. Bennett, C.M. Rienstra, M. Auger, K.V. Lakshmi, R.G. Griffin, J. Chem. Phys. **103**, 6951–6958 (1995)
32. T. Egorova-Zachernyuk, B. van Rossum, C. Erkelens, H. de Groot, Magn. Reson. Chem. **46**, 1074–1083 (2008)
33. M.H.B. Stowell, T.M. McPhillips, D.C. Rees, S.M. Soltis, E. Abresch, G. Feher, Science **276**, 812–816 (1997)
34. S. Stoll, A. Schweiger, J. Magn. Reson. **178**, 42–55 (2006)
35. M. Veshtort, R.G. Griffin, J. Magn. Reson. **178**, 248–282 (2006)
36. M.G. Zysmilich, A. McDermott, Proc. Natl. Acad. Sci. USA. **93**, 6857–6860 (1996)
37. M.R. Fischer, H.J.M. De Groot, J. Raap, C. Winkel, A.J. Hoff, J. Lugtenburg, Biochemistry **31**, 11038 (1992)
38. S. Prakash, Doctoral Thesis, Leiden University, Leiden, The Netherlands, (2006). https://openaccess.leidenuniv.nl/handle/1887/4555
39. R. Kaptein, J. Chem. Soc. D Chem. Comm., **14**, 732–733 (1971)
40. R. Klette, J.T. Torring, M. Plato, K. Möbius, B. Bönigk, W. Lubitz, J. Phys. Chem. **97**, 2015–2020 (1993)
41. P. Dorlet, A.W. Rutherford, S. Un, Biochemistry **39**, 7826–7834 (2000)
42. M.G. Zysmilich, A. McDermott, J. Am. Chem. Soc. **118**, 5867–5873 (1996)
43. F. Lendzian, M. Huber, R.A. Isaacson, B. Endeward, M. Plato, B. Bönigk, K. Möbius, W. Lubitz, G. Feher, Biochim. Biophys. Acta **1183**, 139–160 (1993)
44. A. Diller, S. Prakash, A. Alia, P. Gast, J. Matysik, G. Jeschke, J. Phys. Chem. B **111**, 10606–10614 (2007)
45. H. Kurreck, B. Kirste, W. Lubitz, *Electron Nuclear Double Resonance Spectroscopy of Radicals in Solutions* (VCH, Weinheim, 1988)

46. A. De Groot, A.J. Hoff, R. Debeer, H. Scheer, Chem. Phys. Lett. **113**, 286–290 (1985)
47. A.J. Hoff, A. De Groot, S.A. Dikanov, A.V. Astashkin, Y.D. Tsvetkov, Chem. Phys. Lett. **118**, 40–47 (1985)
48. J. Tang, C.P. Lin, J.R. Norris, J. Chem. Phys. **83**, 4917–4919 (1985)
49. A.V. Astashkin, S.A. Dikanov, Y.D. Tsvetkov, Chem. Phys. Lett. **130**, 337–340 (1986)
50. C.P. Lin, M.K. Bowman, J.R. Norris, J. Chem. Phys. **85**, 56–62 (1986)
51. A.V. Astashkin, S.A. Dikanov, Y.D. Tsvetkov, Chem. Phys. Lett. **152**, 258–264 (1988)
52. I.H. Davis, P. Heathcote, D.J. Maclachlan, M.C.W. Evans, Biochim. Biophys. Acta **1143**, 183–189 (1993)
53. H. Käss, J. Rautter, B. Bonigk, P. Hofer, W. Lubitz, J. Phys. Chem. **99**, 436–448 (1995)
54. F. Lendzian, B. Bonigk, M. Plato, K. Möbius, W. Lubitz, in *The Photosynthetic Bacterial Reaction Center II*, ed. by J. Breton, A. Vermeglio (Plenum Press, New York, 1992), pp. 89–97
55. I.V. Borovykh, S.A. Dzuba, I.I. Proskuryakov, P. Gast, A.J. Hoff, Biochim. Biophys. Acta **1363**, 182–186 (1998)
56. R.E. Blankenship, *Molecular Mechanics of Photosynthesis* (Blackwell Science, Oxford, 2002)
57. S. Santabarbara, I. Kuprov, P.J. Hore, A. Casal, P. Heathcote, M.C.W. Evans, Biochemistry **45**, 7389–7403 (2006)